

## Article

# Vertical Distribution, Diurnal Evolution, and Source Region of Formaldehyde During the Warm Season Under Ozone-Polluted and Non-Polluted Conditions in Nanjing, China

Keqiang Cheng <sup>1</sup>, Mingjie Xie <sup>1,\*</sup>, Yuhang Wang <sup>2</sup> and Yahan Lu <sup>3</sup>

<sup>1</sup> Collaborative Innovation Center of Atmospheric Environment and Equipment Technology, Jiangsu Key Laboratory of Atmospheric Environment Monitoring and Pollution Control, School of Environmental Science and Engineering, Nanjing University of Information Science & Technology, 219 Ningliu Road, Nanjing 210044, China

<sup>2</sup> School of Earth and Atmospheric Sciences, Georgia Institute of Technology, Atlanta, GA 30332, USA; ywang@eas.gatech.edu

<sup>3</sup> Key Laboratory of Land Surface Pattern and Simulation, Institute of Geographic Sciences and Natural Resources Research, CAS, Beijing 100101, China

\* Correspondence: mingjie.xie@nuist.edu.cn

**Abstract:** Formaldehyde (HCHO), a key volatile organic compound (VOC) in the atmosphere, plays a crucial role in driving photochemical processes. Satellite-based observations of column concentrations of HCHO and other gaseous pollutants (e.g., NO<sub>2</sub>) have generally been used in previous studies to elucidate the mechanisms behind secondary organic aerosol (SOA) and ozone (O<sub>3</sub>) formation. This study aimed to investigate the characteristics of HCHO by retrieving its vertical profile over Nanjing during the warm season (May–June 2022) and analyzing the diurnal variation in vertical distribution and potential source regions on non-polluted (MDA8 O<sub>3</sub> < 160 μg m<sup>-3</sup>, NO<sub>3</sub>P) and O<sub>3</sub>-polluted (MDA8 O<sub>3</sub> ≥ 160 μg m<sup>-3</sup>, O<sub>3</sub>P) days. Under both conditions, HCHO was primarily concentrated below 1.5 km altitude, with average vertical profiles displaying similar Boltzmann-like distributions. However, HCHO concentrations on O<sub>3</sub>P days were 1.2–1.6 times higher than those on non-polluted days at the same altitude below 1.5 km. Maximum HCHO concentrations occurred in the afternoon, while the peak value in the 0.1–0.4 km layers was reached around noon (~11:00 a.m.). The variation rates (VR) of HCHO in the 0.3–1.2 km altitudes had a maximum on O<sub>3</sub>P days (approximately 0.33 ppbv h<sup>-1</sup>), and were significantly higher (*p* < 0.01) than the VR observed on NO<sub>3</sub>P days (0.14–0.20 ppbv h<sup>-1</sup>). The analysis of footprints showed that HCHO concentrations were jointly influenced by the upstream region and the surroundings of the study site. The study results improve the understanding of the vertical distribution and potential source regions of HCHO.

**Keywords:** formaldehyde; vertical profile; diurnal evolution; potential source region; MAX-DOAS



**Citation:** Cheng, K.; Xie, M.; Wang, Y.; Lu, Y. Vertical Distribution, Diurnal Evolution, and Source Region of Formaldehyde During the Warm Season Under Ozone-Polluted and Non-Polluted Conditions in Nanjing, China. *Remote Sens.* **2024**, *16*, 4313. <https://doi.org/10.3390/rs16224313>

Academic Editor: Michael Obland

Received: 9 October 2024

Revised: 14 November 2024

Accepted: 16 November 2024

Published: 19 November 2024



**Copyright:** © 2024 by the authors. Licensee MDPI, Basel, Switzerland. This article is an open access article distributed under the terms and conditions of the Creative Commons Attribution (CC BY) license (<https://creativecommons.org/licenses/by/4.0/>).

## 1. Introduction

Volatile organic compounds (VOCs) have garnered significant attention due to their harmful impacts on both human health and the environment [1–3]. Atmospheric VOCs primarily originate from biological processes, human activities, and biomass combustion [4–7]. A considerable number of VOCs are reactive in the atmosphere, playing a crucial role in the formation of SOA and O<sub>3</sub> [7–9]. Over the past decade, air quality improvement policies have been enacted in series in China, resulting in substantial reductions in major pollutants such as particulate matter. However, concentrations of VOCs and O<sub>3</sub> have paradoxically risen [10–13]. The vast diversity of VOCs and their different chemical reactivity present significant challenges in evaluating their atmospheric behavior. Therefore, tracking VOC oxidation products is of great significance to enhancing our current understanding of atmospheric photochemical pollution processes.

Formaldehyde (HCHO) serves as a transient intermediate for the majority of atmospheric VOCs [14–16]. Its primary sources include incomplete combustion and the photochemical oxidation of VOCs [17,18]. HCHO is subject to rapid photolysis and reactions with hydroxyl radicals (OH) [19], and its by-products, such as hydroperoxyl, play a role in the NO-NO<sub>2</sub> cycle [20], ultimately contributing to O<sub>3</sub> formation [17,21,22]. Due to its strong correlation with overall VOC reactivity, HCHO is sometimes used to represent total VOCs [23]. Given that the photolytic reactions of VOCs and NO<sub>2</sub> are critical to the formation of tropospheric O<sub>3</sub>, the ratio of HCHO to NO<sub>2</sub> has been widely employed to evaluate O<sub>3</sub> formation sensitivity [24–27]. Satellite-based observations enable the simultaneous retrieval of HCHO and NO<sub>2</sub> data, aiding studies on the spatial distribution of O<sub>3</sub> formation regimes [26–28]. However, satellite-based observations can only provide the vertical column density (VCD) of HCHO and NO<sub>2</sub> around the overpass time or during the daytime, which may not accurately capture the dynamics of O<sub>3</sub> formation. Furthermore, due to the uneven vertical mixing of atmospheric components in the lower troposphere and transport at different vertical levels, the VCD of HCHO and NO<sub>2</sub> may not reliably indicate O<sub>3</sub> sensitivity at lower atmospheric levels [29]. To better understand tropospheric VOC pollution and O<sub>3</sub> formation, it is crucial to develop ground-based vertical measurements that provide high temporal resolution HCHO data.

The technique of differential optical absorption spectroscopy (DOAS) is frequently used to measure the vertical distribution of atmospheric components (e.g., aerosols and trace gases) [30–33]. Ground-based multi-axis DOAS (MAX-DOAS), in particular, is a technique capable of simultaneously obtaining the vertical distribution of aerosols and trace gases with high temporal resolution [34]. In several prior studies, the integration of ground-based and satellite-based observations has been employed to determine both the column and vertical profiles of HCHO [16,28], which significantly enhances investigations into the formation of atmospheric VOCs and O<sub>3</sub>.

The Yangtze River Delta (YRD), one of the most rapidly developing regions in China, has suffered from severe air pollution in recent years. Despite ongoing efforts to control emissions, the influence of regional pollution transport and secondary pollutants on local air quality has become more apparent. The surface concentrations of major pollutants are significantly impacted by their transport through the troposphere [35–38]. However, in the formulation of pollution control strategies, the focus has primarily been on surface pollutant concentrations, while the vertical distribution and regional origins of air pollutants have been overlooked. This study aimed to (1) measure HCHO's vertical distribution using MAX-DOAS on both O<sub>3</sub>P and NO<sub>3</sub>P days in Nanjing, China; (2) examine temporal variations in the vertical HCHO profile; and (3) explore the potential source regions and their influence on HCHO at different altitudes. The results provide valuable insights into HCHO's role in O<sub>3</sub> formation and its response to varying meteorological conditions, which has implications for atmospheric modeling and air quality management.

## 2. Materials and Methods

### 2.1. Observation Site

Ground-based MAX-DOAS observations were performed on an academic building's rooftop (about 22 m) at Nanjing University of Information Science and Technology (NUIST, Figure 1) from April to June 2022. This site is situated in a suburban setting in northern Nanjing, bordered by residential areas and two major expressways. Notably, large-scale petrochemical facilities are located roughly 6 km northeast of the site. During the observation period, the average daytime temperature was 23.8 °C, with an average humidity of 51.3% and a wind speed of 4.6 m/s.

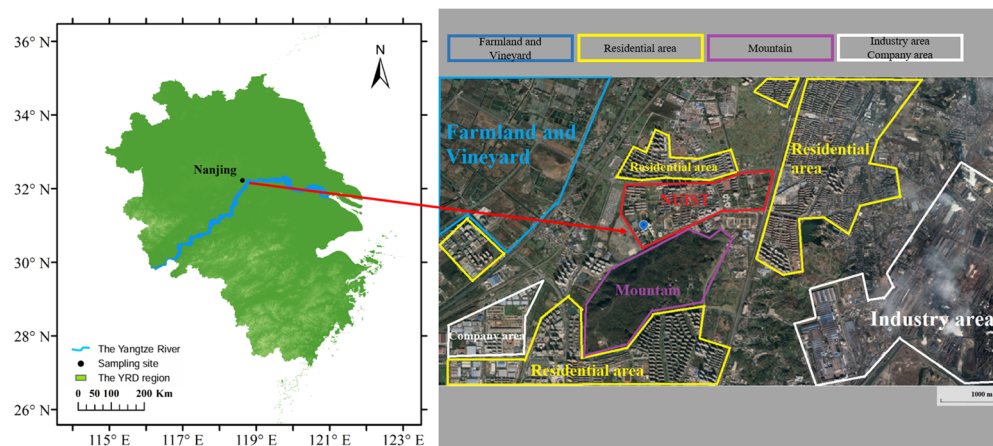


**Figure 1.** Geographical characteristics, location, and surrounding functional areas of NUIST.

### 2.2. Details of Spectral Analysis and Retrieval of Vertical Profile

The MAX-DOAS primarily comprises three components: a scanning telescope unit and two spectrometer units. The elevation angles for measuring scattered sunlight are configured to  $1^\circ$ ,  $2^\circ$ ,  $3^\circ$ ,  $4^\circ$ ,  $5^\circ$ ,  $6^\circ$ ,  $8^\circ$ ,  $10^\circ$ ,  $15^\circ$ ,  $30^\circ$ , and  $90^\circ$ , which takes about 12 min for a full scan. To maintain consistency across observations, each measurement's exposure time is modified based on the scattered light intensity detected with the instrument. Additionally, offset spectra and dark current are recorded during nighttime and subtracted from the daytime spectra to improve accuracy.

Differential slant column densities (DSCDs) were calculated through the analysis of scattered solar spectra using the DOAS technique. The DSCD fitting results were processed with QDOAS software (<https://github.com/UVVIS-BIRA-IASB/qdoas/>, accessed on 27 March 2023). Table 1 outlines the recommended configurations for trace gases' absorption cross-sections and additional DOAS parameters (details in Supplementary Section S1). For each scanning sequence, zenith spectra served as the Fraunhofer reference spectrum for DSCD calculation. To enhance the signal-to-noise ratio and minimize uncertainties in the vertical profile retrievals, spectra with solar zenith angle greater than  $80^\circ$  and DSCDs with residuals of root mean square error (RMSE) exceeding  $6.0 \times 10^{-4}$  were excluded. Figure 2 presents typical spectral results recorded at 10:45 LST on 5 May 2022.

**Table 1.** DOAS fitting configuration for the DSCDs of  $O_4$ ,  $NO_2$ , and HCHO.

Parameter	Refer Data Source	Fitting Interval (nm)	
		$O_4/NO_2$	HCHO
Wavelength range		338–370	322.5–358
NO <sub>2</sub>	298 K <sup>a</sup> [39]	✓	✓
NO <sub>2</sub>	220 K <sup>a</sup> [39]	✓	×
O <sub>3</sub>	223 K <sup>b</sup> [40]	✓	✓
O <sub>3</sub>	243 K <sup>b</sup> [40]	✓	✓
O <sub>4</sub>	293 K [41]	✓	✓
BrO	223 K [42]	✓	✓
HCHO	297 K [43]	✓	✓
Ring	Calculated with QDOAS [44]	✓	✓
Polynomial degree		Order 5	Order 5
Intensity offset		Constant	Constant

a:  $I_0$  correction (SCD of  $10^{17}$  molecules  $cm^{-2}$ ); b:  $I_0$  correction (SCD of  $10^{20}$  molecules  $cm^{-2}$ ).

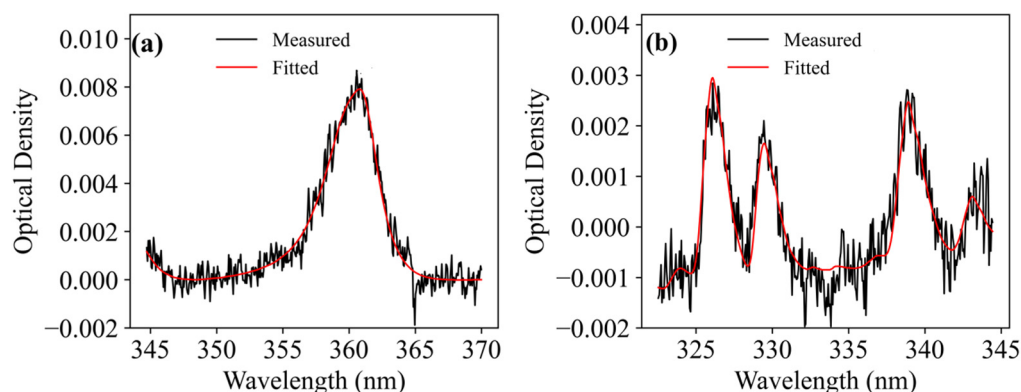


**Figure 2.** A typical fitting result of (a) O<sub>4</sub> and (b) HCHO at 10:45 LST on 5 May 2022.

Vertical profiles were estimated with the optimal estimation method (OEM, details in Supplementary Section S2) [35]. The cost function, which governs the retrieval process, is defined as follows:

$$\chi^2 = [y - F(x, \beta)]^T S_\epsilon^{-1} [y - F(x, \beta)] + [x - x_a] S_a^{-1} [x - x_a]^T \quad (1)$$

here, SCIATRAN version 4.5.5, a widely recognized radiative transfer model, was employed as the forward model, denoted as  $F(x, \beta)$ , where  $x$  is the state vector (i.e., the vertical profile),  $\beta$  refers to the non-retrieved system parameters, and  $y$  is the measurement sequence vector of the DSCDs. The variable  $x_a$  is the a priori profile of the aerosol or trace gas, serving as the initial input for the profile inversion algorithm.  $S_\epsilon$  and  $S_a$  are the uncertainty of  $y$  and  $x_a$ , respectively.

A two-step inversion algorithm was applied to calculate the vertical profiles. Firstly, aerosol extinction (AE) profiles were derived from O<sub>4</sub> DSCDs. Secondly, these AE profiles were used as inputs to calculate trace gases' vertical profiles. In the inversion process, the following fixed aerosol optical properties were assumed: surface albedo of 0.05, single scattering albedo of 0.90, and asymmetry parameter of 0.72 [34]. The troposphere below 4 km was segmented into 31 layers. The first 10 layers below 1.0 km were spaced on a grid of 100 m, while the remaining 21 layers, spanning from 1.0 km to 4.0 km, were spaced on a grid of 200 m. Figure 3 presents exemplary vertical distribution of the AE at 360 nm and HCHO during the observation period. The Boltzmann a priori profiles were used for both aerosols and HCHO. Near-surface aerosol extinction coefficients and HCHO concentrations (in volume mixing ratios, VMR) were set to be 0.3 km<sup>-1</sup> and 5 ppbv, respectively. The degrees of freedom (DOFs) reflect the amount of independent retrievable information in profile inversion [45]. Therefore, only the retrieval results with DOFs > 1.0 were retained in this study.

### 2.3. Potential Source Region Analysis

A particle dispersion model, the Stochastic Time-Inverted Lagrangian Transport Model (STILT, version 2), was employed to simulate the transport of air parcels [46]. In this model, air parcels are represented as ensembles of particles with equal mass, which are transported backward in time from a specific point to upstream regions [47]. The model's footprint is defined as the sensitivity to surface flux, expressed in units of ppb m<sup>2</sup> s μmol<sup>-1</sup>, which indicates the mixing ratio per unit of surface flux. For example, a large footprint value indicates that the surface flux from potential sources significantly influences the concentration of target species at the selected receptor.

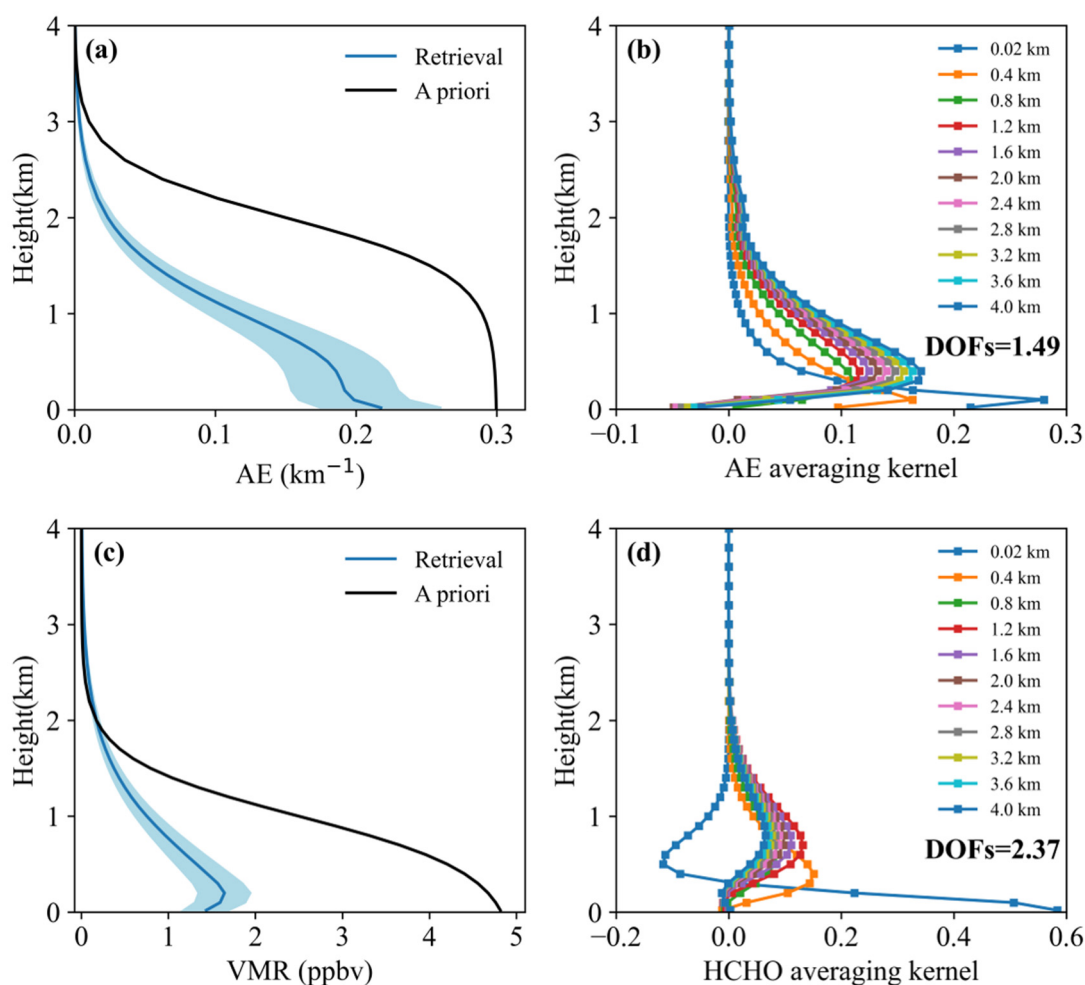


**Figure 3.** Vertical profile examples for the aerosol extinction (AE) coefficient and HCHO at 10:36 LST on 1 May 2022. The left panels (a,c) display the a priori and retrieved profiles of AE and HCHO, while the right panels (b,d) show the averaging kernels and DOFs corresponding to the results. The shadings represent the retrieved errors.

For this study, the analysis product of the Global Forecast System (GFS 0.25°) was used to drive the STILT model. The simulation produced 24-hour backward output footprints, covering the period from 08:00 to 17:00 local time, whose spatial resolution was  $0.02^\circ \times 0.02^\circ$  and an hourly output interval. The receptor point was set at the geographical location of NUIST, and the particle number was fixed at 1000. This particle count represents the ensemble size used for simulating back trajectories [48], and insufficient particle numbers can introduce variability in the simulation results between model runs.

#### 2.4. WRF Configuration and Evaluation

The Weather Research and Forecasting model (WRF version 4.3) was employed to simulate meteorological fields from May to June 2022 over a domain that contains  $89 \times 99$  grid cells in a 27 km horizontal resolution. The European Center for Medium-Range Weather Forecasts (ECMWF) producing ERA5 reanalysis data, whose spatial resolution is  $0.25^\circ \times 0.25^\circ$ , provided the initial and boundary conditions. The detailed information and physical configurations of the WRF model are available in Supplementary Section S3.

To evaluate the value of simulated, the correlation coefficient (R), root mean square error (RMSE), normalized mean error (NME), and mean bias (MB) were adopted (Table 2). The RMSE is calculated by the equation:

$$RMSE = \sqrt{\frac{1}{N} \sum_{n=1}^N [(X_n - \bar{X}) - (X_{obs,n} - \bar{X}_{obs})]^2} \quad (2)$$

where  $N$  is the number of observations,  $X_{obs,n}$  the observations,  $X_n$  the corresponding simulated results,  $\bar{X}$  and  $\bar{X}_{obs}$  are the average values of the simulated result and observation, respectively.

**Table 2.** Comparison of model simulation with actual observations in Nanjing.

Parameter	Month	MB	NME/%	RMSE	R
T <sub>2</sub> (°C)	Apr	0.1	8.5	2.0	0.95
	May	1.2	8.0	2.2	0.90
	Jun	0.1	5.2	1.8	0.90
RH <sub>2</sub> (%)	Apr	−3.0	13.8	10.2	0.88
	May	−8.7	19.7	11.4	0.82
	Jun	−1.6	10.9	9.2	0.84
WS <sub>10</sub> (m/s)	Apr	1.2	38.7	1.2	0.66
	May	0.8	34.1	1.2	0.64
	Jun	0.9	33.0	1.5	0.67

The NME and MB are reported as follows:

$$NME = \frac{\sum_{n=1}^N |X_n - X_{obs,n}|}{\sum_{n=1}^N X_{obs,n}} \times 100\% \quad (3)$$

$$MB = \frac{1}{N} \sum_{n=1}^N |X_n - X_{obs,n}| \quad (4)$$

### 2.5. Ancillary Data

Ozone (O<sub>3</sub>) concentration data were acquired from China National Environmental Monitoring Center (CNEMC), which manages a comprehensive air quality monitoring network with around 1500 stations across 454 cities. The hourly surface O<sub>3</sub> concentration data were collected from a designated CNEMC air monitoring station (ID: 1157A, located at 32.09°N, 118.62°E), situated approximately 10 km from our study site. To ensure data integrity, severe outliers were identified and excluded through the Z-score method as part of the data quality control process.

## 3. Results

### 3.1. Overview of the Observations

Surface O<sub>3</sub> concentrations in the YRD region have increased significantly in warm seasons [49]. Figure 4a shows the proportions of O<sub>3</sub>P and NO<sub>3</sub>P days in Nanjing during April–June 2020–2022, revealing that more than one-third of the days were polluted in the warm season. The hourly average O<sub>3</sub> concentration of pollution days was  $121 \pm 51.0 \mu\text{g m}^{-3}$ , significantly higher than the average on NO<sub>3</sub>P days ( $p < 0.05$ ), which is  $85.3 \pm 35.8 \mu\text{g m}^{-3}$ . Except for primary emissions, secondary formation processes also play a major role in atmospheric HCHO concentrations [50], and the secondary HCHO originates mainly from radical-driven reactions [51]. To further illustrate the relationship between O<sub>3</sub> and HCHO, the boxplots of MDA8 O<sub>3</sub> concentrations in different mixing ratio ranges of near-surface HCHO are shown in Figure 4b. The results indicate a linear increase in MDA8 O<sub>3</sub> concentration with rising HCHO, suggesting that HCHO plays a critical role in O<sub>3</sub>-related photochemical reactions in the atmosphere during the warm season in Nanjing.

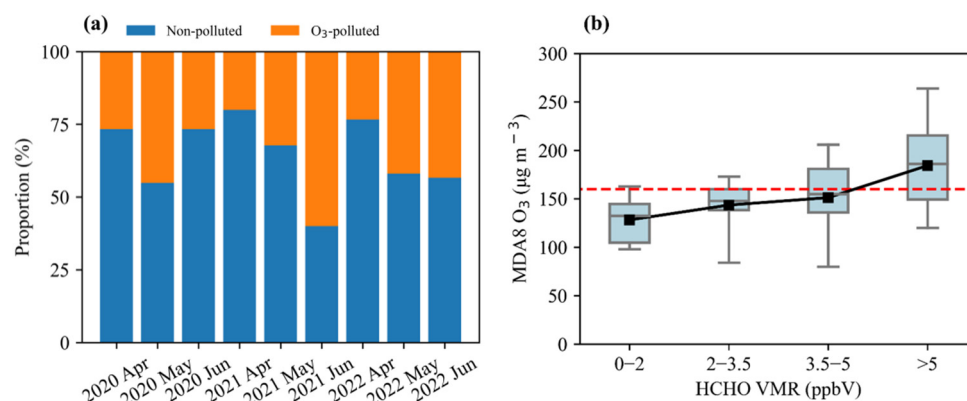
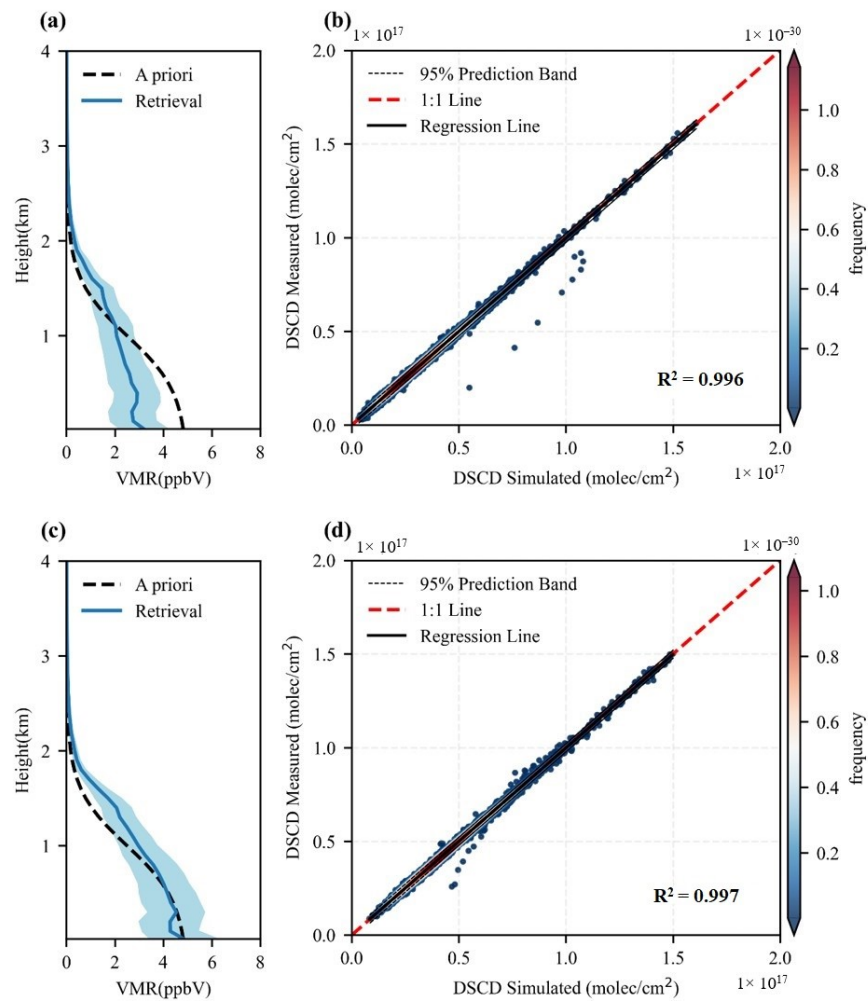


**Figure 4.** (a) Proportions of O<sub>3</sub>P and NO<sub>3</sub>P days in Nanjing from April to June 2020–2022. (b) Box-plots showing MDA8 O<sub>3</sub> concentrations across different HCHO mixing ratio bins over the entire observation period (April to June 2022). The line and black square within the boxes represent the median and mean values, respectively. The upper and lower edges of the box correspond to the 75th and 25th percentiles, while the whiskers extend to the 95th and 5th percentiles. The red dash line represents the MDA8 O<sub>3</sub> equals 160 µg m<sup>-3</sup>.

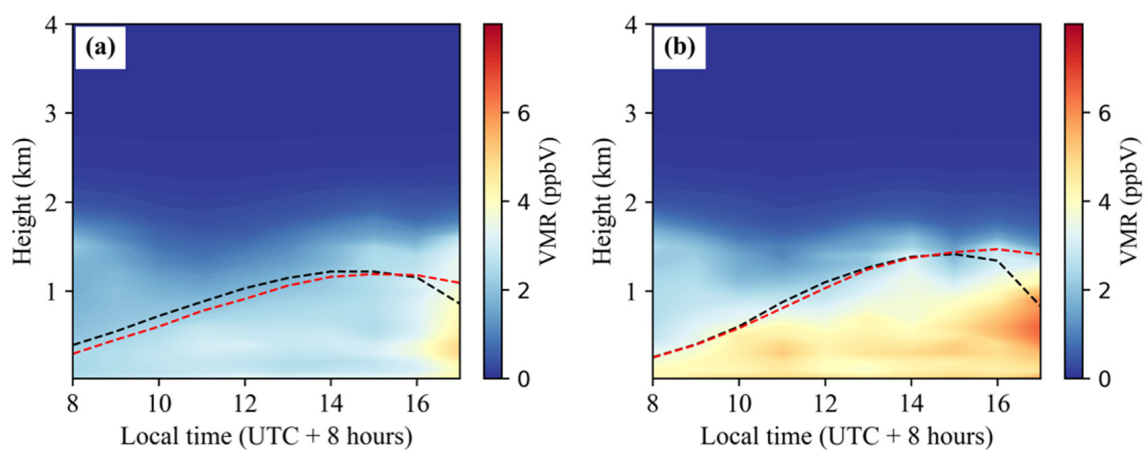
### 3.2. Vertical Distribution of HCHO

Figure 5 presents the average vertical profiles of HCHO for both O<sub>3</sub>P and NO<sub>3</sub>P days, along with a scatter density verification plot comparing the measured and simulated DSCDs. The average vertical profiles of HCHO under the two O<sub>3</sub> conditions are similar (Boltzmann shape, Figure 5a,c). Specifically, HCHO concentration fluctuates below 0.5 km and gradually decreases with increasing altitude. This feature of the HCHO distribution was consistently observed within the 0–2 km altitude range, primarily attributed to local surface emissions and photochemical processes occurring in the lower troposphere [52]. Comparing HCHO's vertical profiles under these two conditions, the average HCHO concentration below 1.5 km was 1.2–1.6 times greater on O<sub>3</sub>P days than on NO<sub>3</sub>P days. Although the distributions of HCHO at higher altitudes (>1.5 km) were similar, the vertical column density (VCD) of HCHO below 1.5 km on O<sub>3</sub>P days ( $1.04\text{--}1.39 \times 10^{16}$  molecules cm<sup>-2</sup>) was higher than the VCD on NO<sub>3</sub>P days ( $6.24\text{--}9.37 \times 10^{15}$  molecules cm<sup>-2</sup>). In this study, the observation site is situated in the YRD region, which is influenced by the subtropical high-pressure system of the western Pacific Ocean in the warm season, leading to strong convective activity and horizontal transport. Long-term monitoring of trace gases such as HCHO, SO<sub>2</sub>, and NO<sub>2</sub> in typical YRD cities indicates that meteorological conditions significantly influence their transport and distribution [53,54].

Figure 6 presents the average diurnal variations in the HCHO vertical profiles for both O<sub>3</sub>P and NO<sub>3</sub>P days. Notably, HCHO concentrations were predominantly concentrated below 2 km under both conditions. Due to the close relationship between HCHO and the photochemical reactions in the atmosphere, higher HCHO concentrations usually occur at midday or late afternoon [55]. The HCHO concentration reached its maximum during 16:00–17:00 on NO<sub>3</sub>P days and remained at a low level before 16:00 (Figure 6a). On O<sub>3</sub>P days, HCHO concentrations below 1 km were significantly higher ( $p < 0.05$ ). HCHO rapidly accumulated within the BL (Figure 6b), the height of which increased from approximately 400 to 900 m from sunrise until noon. The peak concentrations (approximately 4.03–5.48 ppbv) were also observed in layers 0.3–1.0 km high during 16:00–17:00, as elevated O<sub>3</sub> levels and intense solar radiation facilitated the formation of secondary HCHO. It is noteworthy that the HCHO concentration in 1–1.5 km high layers initially decreased a little and then increased. One possible explanation is that the high HCHO concentrations in the morning were primarily caused by the accumulation of previously formed HCHO under stable weather conditions during the night. After sunrise, the photolysis of HCHO increased, and the boundary layer height increased to more than 1 km at noon, enabling well-mixed conditions below.



**Figure 5.** Vertical distribution of HCHO on  $\text{NO}_3\text{P}$  days (a) and on  $\text{O}_3\text{P}$  days (c) over the entire period and the corresponding scatter density verification diagram of measured and simulated DSCDs (b,d). The shadings represent the mean retrieved errors.



**Figure 6.** Average diurnal variations in the vertical distribution of HCHO on (a)  $\text{NO}_3\text{P}$  days and on (b)  $\text{O}_3\text{P}$  days. The black and red dash lines are the BL height of ERA5 and WRF modeled, respectively.

### 3.3. The Variation Rates of HCHO Concentrations at Different Altitudes

Figure 7 illustrates the variation rates (VR) of HCHO concentrations at different altitudes derived from hourly observations. Moreover, the retrieval results of HCHO concentrations at altitudes of 0.02 km, 0.6 km, and 1 km were regressed on the time of day, which underscores the significant temporal variation of HCHO concentrations throughout the daytime (correlation coefficients ranged from 0.77 to 0.99, Figure 7b–d,f–h). Compared to the stable and low concentrations in the upper troposphere, daytime HCHO concentrations below 2 km increased both on O<sub>3</sub>P and NO<sub>3</sub>P days. The VR of HCHO on NO<sub>3</sub>P days remained at  $0.19 \pm 0.02$  ppbv h<sup>-1</sup> between 0.3 km and 1.5 km altitude. At altitudes higher than 1.5 km, the VR decreased rapidly to 10<sup>-4</sup> ppbv h<sup>-1</sup>. Although the vertical pattern of VR on O<sub>3</sub>P days differed from that on NO<sub>3</sub>P days, the high VR occurred in the same altitude range (Figure 7a,e). The variation rate reached its maximum (0.34 ppbv h<sup>-1</sup>) at an altitude of 600 m and decreased rapidly above and below this altitude. This vertical pattern on O<sub>3</sub>P days can be attributed to local convective transport, as shown by the high concentrations and low variation rates near the ground (Figures 6b and 7e). Notably, the negative VR at 1.6–2 km altitude on O<sub>3</sub>P days suggests nocturnal advective transport in the upper boundary layer, leading to the accumulation of HCHO. This accumulation with subsequent deposition possibly contributes to the peak observed at 0.3–1 km altitude.

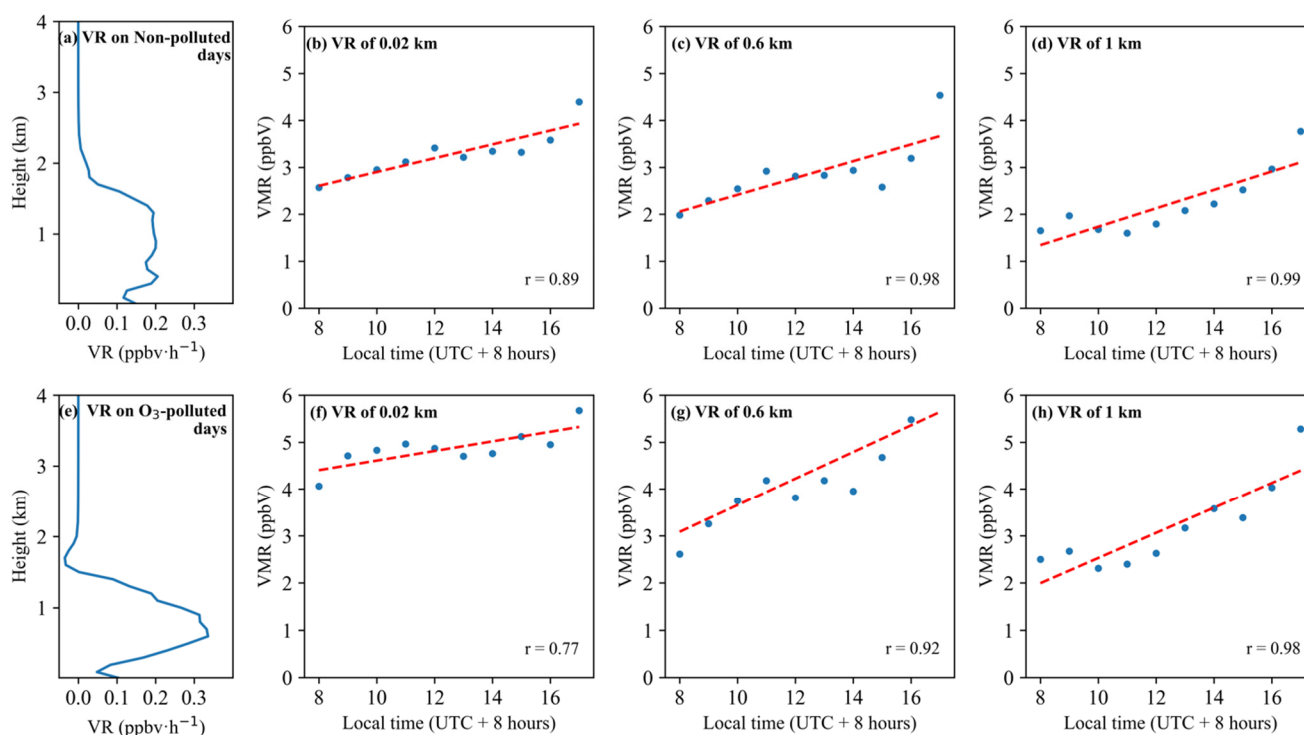


**Figure 7.** Vertical pattern of HCHO variation rates on (a) NO<sub>3</sub>P days, linear regressions and correlation coefficients between hourly HCHO concentrations and time of day at altitudes of (b) 0.02 km, (c) 0.6 km, and (d) 1 km, the corresponding analysis for O<sub>3</sub>P days as (e–h).

## 4. Discussion

### 4.1. The Relationship Between HCHO Concentrations and Meteorological Parameters at Different Altitudes

As shown in Table 3, the relationship between HCHO concentration at different altitudes and meteorological factors—temperature (T), relative humidity (RH), and wind speed (WS)—exhibited distinct characteristics under NO<sub>3</sub>P and O<sub>3</sub>P days. On NO<sub>3</sub>P days, a notable positive correlation between HCHO and temperature at different altitudes, indicating that elevated temperatures facilitate HCHO formation when ambient O<sub>3</sub> is low. Conversely, the relationship between HCHO concentrations and meteorological parameters

on O<sub>3</sub>-polluted days exhibited greater complexity. Atmospheric conditions with high temperatures and high humidity in the near-surface layers (below 0.6 km) had a notable impact on HCHO formation, partly due to the greater formation of hydroxyl radicals (OH), which can react with VOCs to produce formaldehyde [55,56]. Additionally, the correlation between HCHO concentration and wind speed suggests that pollutant transport alone may not be the primary factor driving high HCHO levels on O<sub>3</sub>P days; instead, localized emissions or photochemical production could contribute to elevated HCHO concentrations under low-wind conditions.

**Table 3.** Correlation analysis of HCHO with meteorological parameters on O<sub>3</sub>P and NO<sub>3</sub>P days.

Parameter	Altitude	T (°C)	RH (%)	WS (m/s)
NO <sub>3</sub> P days	surface	0.74 **	0.04	−0.03
	0.6 km	0.69 **	0.10	−0.03
	1 km	0.69 **	−0.10	−0.11
O <sub>3</sub> P days	surface	0.53 **	0.55 **	−0.30
	0.6 km	0.50 **	0.53 **	−0.30
	1 km	0.42 *	0.10	−0.44 *

\*\*  $p < 0.01$ ; \*  $p < 0.05$ .

#### 4.2. Source Region and Their Impacts on HCHO at Different Altitudes

Based on the aforementioned results, three altitudes—0.02 km, 0.6 km, and 1 km—were selected to evaluate the source regions and their influences under both conditions. Figures 8 and 9 show the average hourly footprints on O<sub>3</sub>P and NO<sub>3</sub>P days at an altitude of 0.02 km (near the ground). The area of the footprint decreased with time for both conditions, indicating that the maximum concentration in the afternoon (Figure 6) is mainly affected by the region adjacent to the NUIST site. As shown in Figure 8, the footprints on O<sub>3</sub>P days show that the potential sources of HCHO are mainly from the northeast, east, and southeast of NUIST. The area with high footprint values ( $>0.8 \text{ ppb} \cdot \text{m}^2 \cdot \text{s} \cdot \mu\text{mol}^{-1}$ ) was adjacent to the NUIST, indicating a stagnant air mass. On NO<sub>3</sub>P days, the potential HCHO sources were mainly from the northeast and southwest, and the area with high footprint values was much larger. These results suggest that the air mass was transported over long distances with strong northeast or southwest winds on NO<sub>3</sub>P days, and the near-ground concentration of HCHO was related to wind speed.

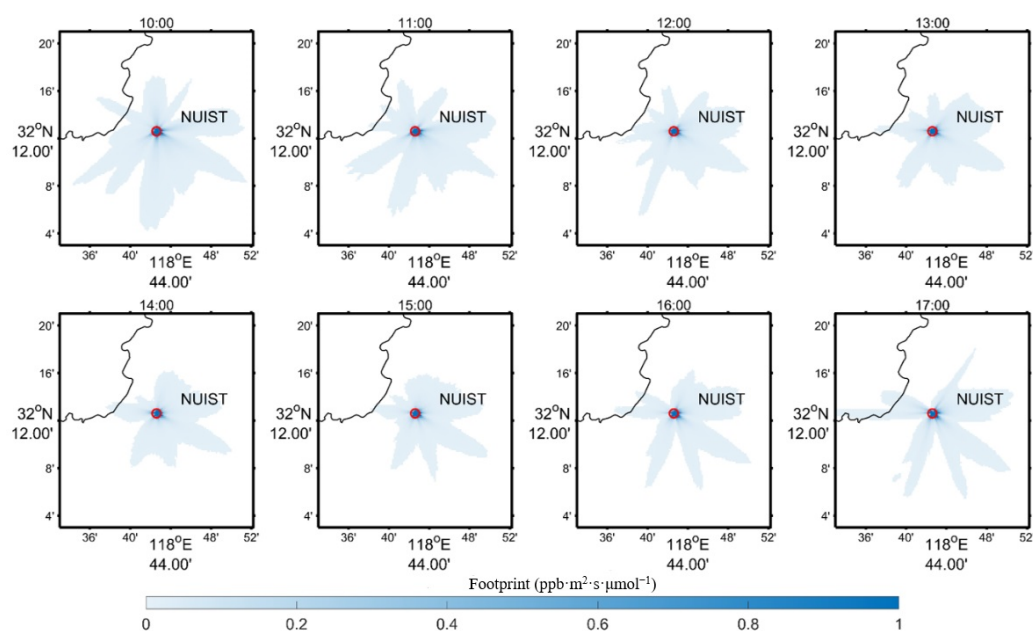


**Figure 8.** Hourly average footprint during the day at 0.02 km altitude on O<sub>3</sub>P days.

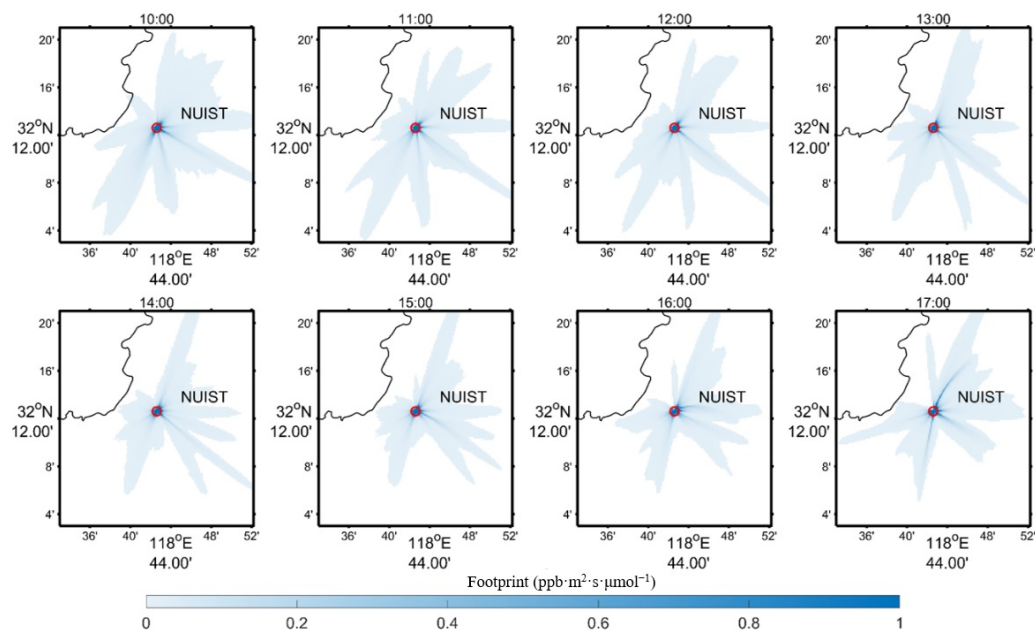


**Figure 9.** Hourly average footprint during the day at 0.02 km altitude on  $\text{NO}_3\text{P}$  days.

In Figure 10, the footprint at 0.6 km altitude on  $\text{O}_3\text{P}$  days shows potential sources originating mainly from the northeastern, eastern, and southeastern regions of NUIST. Compared to the  $\text{O}_3\text{P}$  days, the area of footprints on  $\text{NO}_3\text{P}$  days (Figure 11) was much smaller, suggesting that meteorological conditions on  $\text{NO}_3\text{P}$  days were not conducive to the transport of air masses at this altitude. The value of footprints near the NUIST on  $\text{O}_3\text{P}$  days ( $0.13 \pm 0.06 \text{ ppb m}^2 \text{ s } \mu\text{mol}^{-1}$ ) was comparable to the value for  $\text{NO}_3\text{P}$  days ( $0.12 \pm 0.04 \text{ ppb m}^2 \text{ s } \mu\text{mol}^{-1}$ ), but the value in the period from 10:00–12:00 was higher on  $\text{O}_3\text{P}$  days ( $0.14 \pm 0.07 \text{ ppb m}^2 \text{ s } \mu\text{mol}^{-1}$ ) compared to  $\text{NO}_3\text{P}$  days ( $0.11 \pm 0.03 \text{ ppb m}^2 \text{ s } \mu\text{mol}^{-1}$ ). This suggests that the peak HCHO concentration at 0.6 km altitude at noon may be attributed to a local contribution. Due to the nearly identical footprint values in the period from 15:00–17:00 ( $0.12 \pm 0.03$  for  $\text{NO}_3\text{P}$  and  $0.12 \pm 0.04 \text{ ppb m}^2 \text{ s } \mu\text{mol}^{-1}$  for  $\text{O}_3\text{P}$  days), the observed peak HCHO concentrations in the afternoon warrant further investigation. This can be achieved by quantifying the transport contributions from actual emissions across the entire source region [47]. Additionally, combining this analysis with an atmospheric chemical model to calculate HCHO production and loss will help further explore the underlying causes of this phenomenon. The distribution patterns of potential source regions near the ground and at an altitude of 0.6 km on  $\text{O}_3\text{P}$  days were similar, and this characteristic was also observed on  $\text{NO}_3\text{P}$  days. However, the area and footprint value of the potential source region at 0.6 km were significantly reduced ( $p < 0.05$ ) compared to those near the ground. This difference may be related to variations in boundary layer height throughout the day ( $946.63 \pm 484.61 \text{ m}$  on  $\text{O}_3\text{P}$  days,  $916.47 \pm 397.16 \text{ m}$  on  $\text{O}_3\text{P}$  days). When the boundary layer height was below 0.6 km, the HCHO content in the passing air masses was lower. When the boundary layer height is below 0.6 km, the HCHO content in the air masses passing through this height is lower; as the boundary layer height increases, the HCHO content in the air masses begins to rise due to the influence of emissions and vertical mixing [17,19], with the maximum VR observed at 0.6 km.

The footprints on  $\text{O}_3\text{P}$  and  $\text{NO}_3\text{P}$  days at an altitude of 1 km are shown in Figures 12 and 13. On  $\text{O}_3\text{P}$  days, the northeastern, southwestern, and southeast regions of NUIST were identified as the main potential sources of HCHO. The variation in the potential source area underwent three distinct stages: increasing (10:00–12:00), maintaining (12:00–16:00), and decreasing (16:00–17:00). On  $\text{NO}_3\text{P}$  days, the potential sources were similarly distributed in the northeast and southwest of NUIST, with a similar pattern of variation as on  $\text{O}_3\text{P}$  days. However, the footprint area on  $\text{NO}_3\text{P}$  days was smaller than on  $\text{O}_3\text{P}$  days, which

could explain the lower HCHO concentrations on  $\text{NO}_3\text{P}$  days. The variation pattern of the potential source area at 1 km altitude differed from that of the ground level on both  $\text{O}_3\text{P}$  and  $\text{NO}_3\text{P}$  days. During the period from 12:00 to 16:00 on  $\text{O}_3\text{P}$  days, the area of potential source region and footprint values at 1 km altitude were larger, suggesting that regional transport and localized emissions substantially affect HCHO levels in the upper boundary layer [57,58].

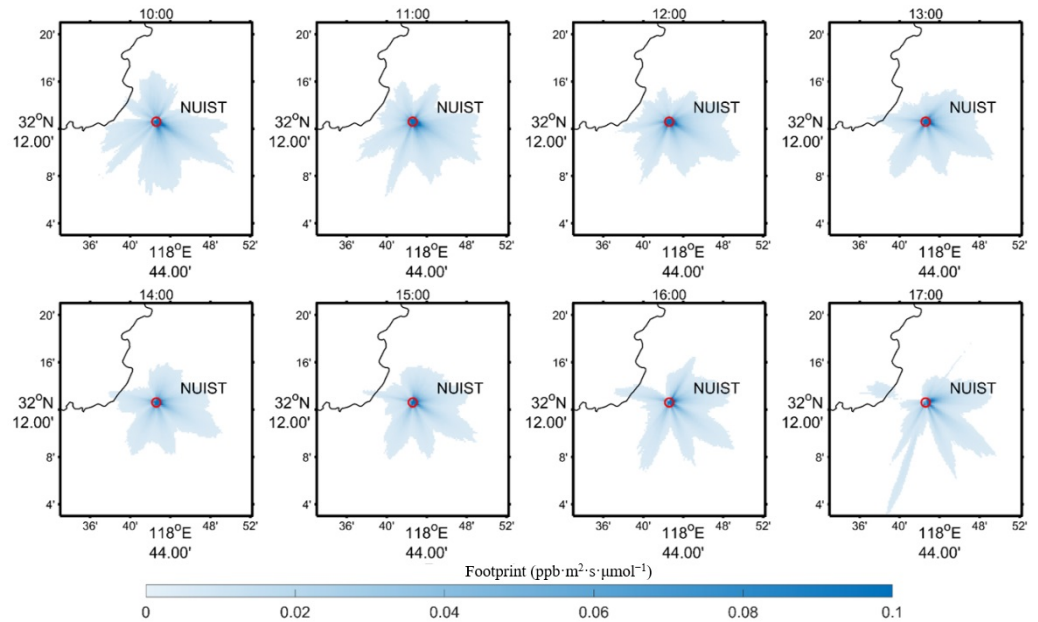


**Figure 10.** Hourly average footprint during the day at 0.6 km altitude on  $\text{O}_3\text{P}$  days.

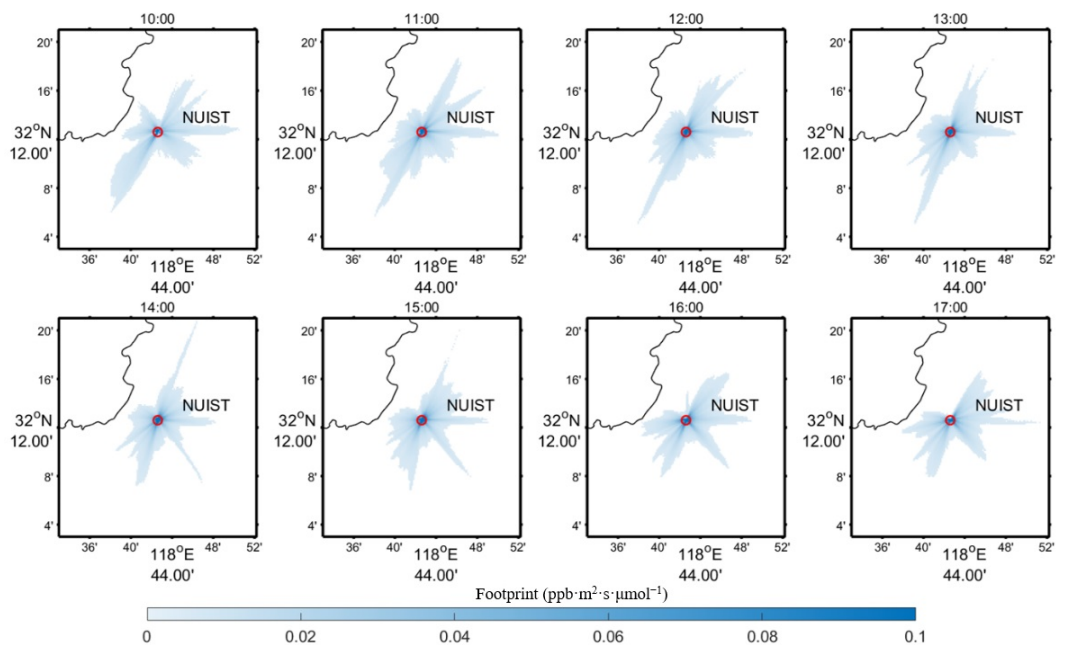


**Figure 11.** Hourly average footprint during the day at 0.6 km altitude on  $\text{NO}_3\text{P}$  days.

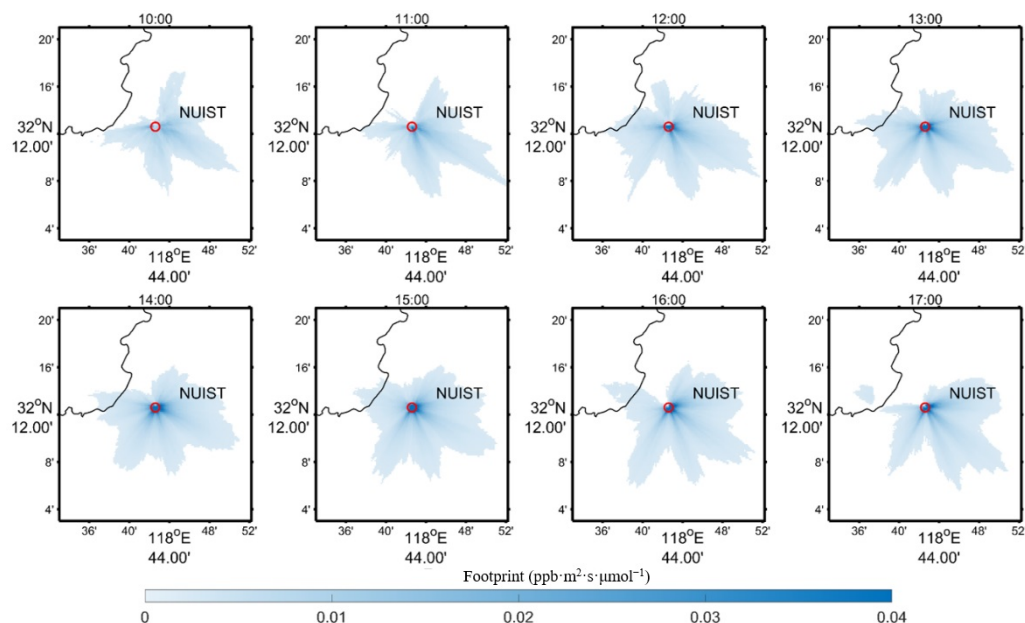


**Figure 12.** Hourly average footprint during the day at 1 km altitude on O<sub>3</sub>P days.

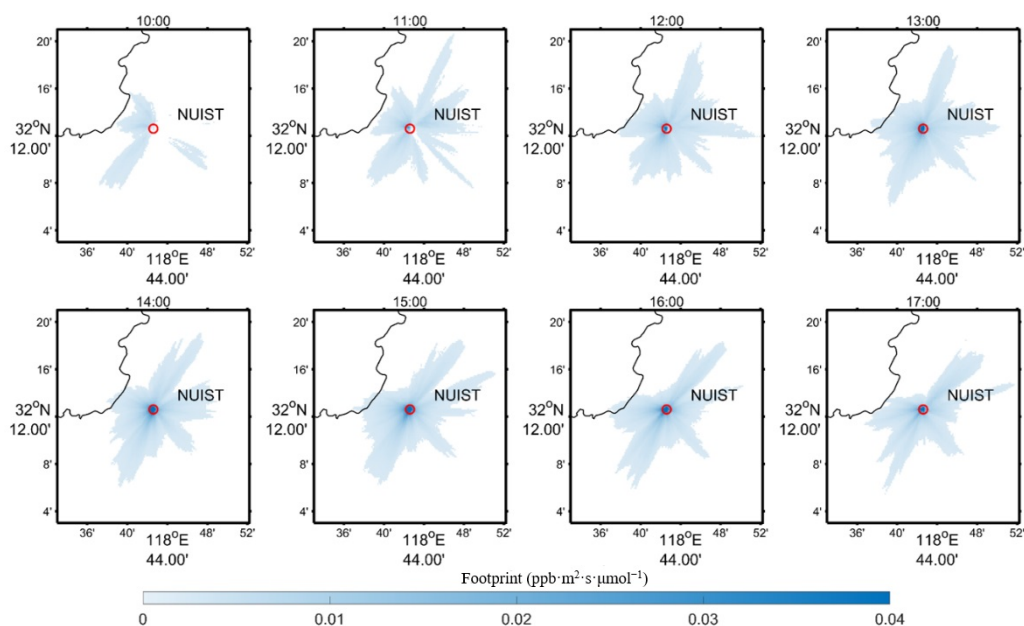


**Figure 13.** Hourly average footprint during the day at 1 km altitude on NO<sub>3</sub>P days.

## 5. Conclusions

In this study, ground-based MAX-DOAS observations and STILT simulations were combined to investigate the vertical distribution, diurnal evolution, and source regions of HCHO during the warm season under O<sub>3</sub>P and NO<sub>3</sub>P conditions in Nanjing, China. The vertical profiles of HCHO exhibited a similar structure across both conditions; however, HCHO concentrations were 1.2 to 1.6 times higher on O<sub>3</sub>P days compared to NO<sub>3</sub>P days at altitudes below 1.5 km. The HCHO concentration on NO<sub>3</sub>P days exhibited a continuous slow increase during the day and reached its maximum in the afternoon, while the HCHO concentration increased sharply and occurred at a peak of 0.3–1.0 km on O<sub>3</sub>P days.

The VR of HCHO concentrations in the 0.3–1.5 km layers on NO<sub>3</sub>P days remained at  $0.19 \pm 0.02$  ppbv h<sup>-1</sup>, suggesting that the synergistic contributions of direct emissions, photochemical production, and transport to HCHO concentrations are consistent throughout the day. In contrast, there was a peak value ( $0.34$  ppbv h<sup>-1</sup>) at 0.6 km on O<sub>3</sub>P days.

The negative variation rate at 1.6–2 km altitude on O<sub>3</sub>P days indicates nocturnal advective transport of HCHO in the upper boundary layer and subsequent deposition. The potential source regions at near-ground and 0.6 km on O<sub>3</sub>P days were mainly from the northeast, east, and southeast of NUIST, while the potential sources on NO<sub>3</sub>P days were ascribed to the northeast and southwest regions. To enable a clearer comparison of source region differences under the two conditions, the study quantifies their influence. On O<sub>3</sub>P days, the area of regions contributing to transport was larger at 0.6 km than on NO<sub>3</sub>P days, and the footprint values near the NUIST at noon ( $0.14 \pm 0.07 \text{ ppb m}^2 \text{ s } \mu\text{mol}^{-1}$ ) were higher than on NO<sub>3</sub>P days ( $0.11 \pm 0.03 \text{ ppb m}^2 \text{ s } \mu\text{mol}^{-1}$ ), which explained the occurrence of peak and maximum concentrations caused by local transport. For the 1 km layer, the potential source regions for both O<sub>3</sub>P and NO<sub>3</sub>P days were mainly distributed in the northeast and southwest of NUIST. The smaller footprint area in the early daytime hours and the variation patterns of increasing–maintaining–decreasing suggest that the high HCHO concentration is related to the nocturnal accumulation of locally formed HCHO and diurnal transport. Since the inversion results are primarily derived from sunny conditions, the findings of this study may not fully represent the dynamics of HCHO during cloudy or rainy days. Furthermore, the absence of multi-source, high-resolution emission data limits the ability to precisely quantify the influence of potential source regions on HCHO. Future studies are warranted to optimize the inversion algorithm and quantify the regional contribution to air pollutants.

**Supplementary Materials:** The following supporting information can be downloaded at: <https://www.mdpi.com/article/10.3390/rs16224313/s1>.

**Author Contributions:** Conceptualization, K.C., M.X. and Y.W.; methodology, K.C.; software, K.C.; formal analysis, K.C.; investigation, K.C.; data curation, K.C. and Y.L.; writing—original draft, K.C.; writing—review and editing, M.X. and Y.W.; supervision, M.X. and Y.W.; project administration, M.X. and Y.W.; funding acquisition, M.X. and Y.W. All authors have read and agreed to the published version of the manuscript.

**Funding:** This research was funded by the National Natural Science Foundation of China (NSFC, 42177211).

**Data Availability Statement:** The data presented in this study are available on request from the corresponding author.

**Acknowledgments:** We would like to express our gratitude to all developers involved in the creation of the STILT model. Special thanks to NCEP for providing the Global Forecast System (GFS) data. The spectrum fitting was conducted using QDOAS, a free and open-source software developed by the authors (<https://github.com/UVVIS-BIRA-IASB/qdoas/>, accessed on 27 March 2023). We are also thankful for the significant contributions made by the SCIATRAN team. We appreciate the CNEMC sites for supplying free hourly trace gas concentration data.

**Conflicts of Interest:** The authors declare no conflicts of interest.

## References

1. Shen, L.; Jacob, D.J.; Liu, X.; Huang, G.; Li, K.; Liao, H.; Wang, T. An Evaluation of the Ability of the Ozone Monitoring Instrument (OMI) to Observe Boundary Layer Ozone Pollution across China: Application to 2005–2017 Ozone Trends. *Atmos. Chem. Phys.* **2019**, *19*, 6551–6560. [[CrossRef](#)]
2. Lu, X.; Hong, J.; Zhang, L.; Cooper, O.R.; Schultz, M.G.; Xu, X.; Wang, T.; Gao, M.; Zhao, Y.; Zhang, Y. Severe Surface Ozone Pollution in China: A Global Perspective. *Environ. Sci. Technol. Lett.* **2018**, *5*, 487–494. [[CrossRef](#)]
3. Yang, W.; Chen, H.; Wang, W.; Wu, J.; Li, J.; Wang, Z.; Zheng, J.; Chen, D. Modeling Study of Ozone Source Apportionment over the Pearl River Delta in 2015. *Environ. Pollut.* **2019**, *253*, 393–402. [[CrossRef](#)] [[PubMed](#)]
4. Barletta, B.; Meinardi, S.; Sherwood Rowland, F.; Chan, C.-Y.; Wang, X.; Zou, S.; Yin Chan, L.; Blake, D.R. Volatile Organic Compounds in 43 Chinese Cities. *Atmos. Environ.* **2005**, *39*, 5979–5990. [[CrossRef](#)]
5. An, J.; Zhu, B.; Wang, H.; Li, Y.; Lin, X.; Yang, H. Characteristics and Source Apportionment of VOCs Measured in an Industrial Area of Nanjing, Yangtze River Delta, China. *Atmos. Environ.* **2014**, *97*, 206–214. [[CrossRef](#)]

6. Baudic, A.; Gros, V.; Sauvage, S.; Locoge, N.; Sanchez, O.; Sarda-Estève, R.; Kalogridis, C.; Petit, J.-E.; Bonnaire, N.; Baisnée, D.; et al. Seasonal Variability and Source Apportionment of Volatile Organic Compounds (VOCs) in the Paris Megacity (France). *Atmos. Chem. Phys.* **2016**, *16*, 11961–11989. [[CrossRef](#)]
7. Xie, M.; Shu, L.; Wang, T.; Liu, Q.; Gao, D.; Shu, L.; Zhuang, B.; Han, Y.; Li, M.; Chen, P. Natural Emissions under Future Climate Condition and Their Effects on Surface Ozone in the Yangtze River Delta Region, China. *Atmos. Environ.* **2017**, *150*, 162–180. [[CrossRef](#)]
8. Dieu Hien, V.T.; Lin, C.; Thanh, V.C.; Kim Oanh, N.T.; Thanh, B.X.; Weng, C.-E.; Yuan, C.-S.; Rene, E.R. An Overview of the Development of Vertical Sampling Technologies for Ambient Volatile Organic Compounds (VOCs). *J. Environ. Manag.* **2019**, *247*, 401–412. [[CrossRef](#)] [[PubMed](#)]
9. Huang, X.; Ding, A.; Gao, J.; Zheng, B.; Zhou, D.; Qi, X.; Tang, R.; Ren, C.; Nie, W.; Chi, X. Enhanced Secondary Pollution Offset Reduction of Primary Emissions during COVID-19 Lockdown in China. *Natl. Sci. Rev.* **2021**, *8*, nwa137. [[CrossRef](#)]
10. Simon, H.; Reff, A.; Wells, B.; Xing, J.; Frank, N. Ozone Trends Across the United States over a Period of Decreasing NO<sub>x</sub> and VOC Emissions. *Environ. Sci. Technol.* **2015**, *49*, 186–195. [[CrossRef](#)]
11. Yan, Y.; Pozzer, A.; Ojha, N.; Lin, J.; Lelieveld, J. Analysis of European Ozone Trends in the Period 1995–2014. *Atmos. Chem. Phys.* **2018**, *18*, 5589–5605. [[CrossRef](#)]
12. Zheng, B.; Tong, D.; Li, M.; Liu, F.; Hong, C.; Geng, G.; Li, H.; Li, X.; Peng, L.; Qi, J.; et al. Trends in China's Anthropogenic Emissions since 2010 as the Consequence of Clean Air Actions. *Atmos. Chem. Phys.* **2018**, *18*, 14095–14111. [[CrossRef](#)]
13. Zhao, Q.; Bi, J.; Liu, Q.; Ling, Z.; Shen, G.; Chen, F.; Qiao, Y.; Li, C.; Ma, Z. Sources of Volatile Organic Compounds and Policy Implications for Regional Ozone Pollution Control in an Urban Location of Nanjing, East China. *Atmos. Chem. Phys.* **2020**, *20*, 3905–3919. [[CrossRef](#)]
14. Sillman, S. The Relation between Ozone, NO<sub>x</sub> and Hydrocarbons in Urban and Polluted Rural Environments. *Atmos. Environ.* **1999**, *33*, 1821–1845. [[CrossRef](#)]
15. Kleinman, L. The Dependence of Tropospheric Ozone Production Rate on Ozone Precursors. *Atmos. Environ.* **2005**, *39*, 575–586. [[CrossRef](#)]
16. Hong, Q.; Liu, C.; Hu, Q.; Zhang, Y.; Xing, C.; Su, W.; Ji, X.; Xiao, S.-H. Evaluating the Feasibility of Formaldehyde Derived from Hyperspectral Remote Sensing as a Proxy for Volatile Organic Compounds. *Atmos. Res.* **2021**, *264*, 105777. [[CrossRef](#)]
17. Luecken, D.; Hutzell, W.; Strum, M.; Pouliot, G. Regional Sources of Atmospheric Formaldehyde and Acetaldehyde, and Implications for Atmospheric Modeling. *Atmos. Environ.* **2012**, *47*, 477–490. [[CrossRef](#)]
18. Huang, C.; Wang, H.L.; Li, L.; Wang, Q.; Lu, Q.; de Gouw, J.A.; Zhou, M.; Jing, S.A.; Lu, J.; Chen, C.H. VOC Species and Emission Inventory from Vehicles and Their SOA Formation Potentials Estimation in Shanghai, China. *Atmos. Chem. Phys.* **2015**, *15*, 11081–11096. [[CrossRef](#)]
19. Sivakumaran, V.; Hölscher, D.; Dillon, T.J.; Crowley, J.N. Reaction between OH and HCHO: Temperature Dependent Rate Coefficients (202–399 K) and Product Pathways (298 K). *Phys. Chem. Chem. Phys.* **2003**, *5*, 4821–4827. [[CrossRef](#)]
20. McKee, K.; Blitz, M.A.; Pilling, M.J. Temperature and Pressure Studies of the Reactions of CH<sub>3</sub>O<sub>2</sub>, HO<sub>2</sub>, and 1,2-C<sub>4</sub>H<sub>9</sub>O<sub>2</sub> with NO<sub>2</sub>. *J. Phys. Chem.* **2016**, *120*, 1408–1420. [[CrossRef](#)]
21. Parrish, D.D.; Ryerson, T.B.; Mellqvist, J.; Johansson, J.; Fried, A.; Richter, D.; Walega, J.G.; Washenfelder, R.A.; de Gouw, J.A.; Peischl, J.; et al. Primary and Secondary Sources of Formaldehyde in Urban Atmospheres: Houston Texas Region. *Atmos. Chem. Phys.* **2012**, *12*, 3273–3288. [[CrossRef](#)]
22. Mellouki, A.; Wallington, T.J.; Chen, J. Atmospheric Chemistry of Oxygenated Volatile Organic Compounds: Impacts on Air Quality and Climate. *Chem. Rev.* **2015**, *115*, 3984–4014. [[CrossRef](#)]
23. Kleinman, L.I.; Daum, P.H.; Lee, J.H.; Lee, Y.; Nunnermacker, L.J.; Springston, S.R.; Newman, L.; Weinstein-Lloyd, J.; Sillman, S. Dependence of Ozone Production on NO and Hydrocarbons in the Troposphere. *Geophys. Res. Lett.* **1997**, *24*, 2299–2302. [[CrossRef](#)]
24. Duncan, B.N.; Yoshida, Y.; Olson, J.R.; Sillman, S.; Martin, R.V.; Lamsal, L.N.; Hu, Y.; Pickering, K.; Retscher, C.; Allen, D.J.; et al. Application of OMI Observations to a Space-Based Indicator of NO<sub>x</sub> and VOC Controls on Surface Ozone Formation. *Atmos. Environ.* **2010**, *44*, 2213–2223. [[CrossRef](#)]
25. Jin, X.; Fiore, A.M.; Murray, L.T.; Valin, L.C.; Lamsal, L.N.; Duncan, B.; Boersma, K.F.; De Smedt, I.; Abad, G.G.; Chance, K.; et al. Evaluating a Space-Based Indicator of Surface Ozone-NO<sub>x</sub>-VOC Sensitivity Over Midlatitude Source Regions and Application to Decadal Trends. *J. Geophys. Res. Atmos.* **2017**, *122*, 10439–10461. [[CrossRef](#)]
26. Jin, X.; Fiore, A.; Boersma, K.F.; Smedt, I.D.; Valin, L. Inferring Changes in Summertime Surface Ozone-NO<sub>x</sub>-VOC Chemistry over U.S. Urban Areas from Two Decades of Satellite and Ground-Based Observations. *Environ. Sci. Technol.* **2020**, *54*, 6518–6529. [[CrossRef](#)] [[PubMed](#)]
27. Liu, J.; Li, X.; Tan, Z.; Wang, W.; Yang, Y.; Zhu, Y.; Yang, S.; Song, M.; Chen, S.; Wang, H.; et al. Assessing the Ratios of Formaldehyde and Glyoxal to NO<sub>2</sub> as Indicators of O<sub>3</sub>-NO<sub>x</sub>-VOC Sensitivity. *Environ. Sci. Technol.* **2021**, *55*, 10935–10945. [[CrossRef](#)]
28. Luo, Y.; Dou, K.; Fan, G.J.; Huang, S.; Si, F.; Zhou, H.; Wang, Y.; Pei, C.; Tang, F.; Yang, D.; et al. Vertical Distributions of Tropospheric Formaldehyde, Nitrogen Dioxide, Ozone and Aerosol in Southern China by Ground-Based MAX-DOAS and LIDAR Measurements during PRIDE-GBA 2018 Campaign. *Atmos. Environ.* **2020**, *226*, 117384. [[CrossRef](#)]

29. Schroeder, J.; Crawford, J.H.; Fried, A.; Weinheimer, A.J. New Insights into the Column CH<sub>2</sub>O/NO<sub>2</sub> Ratio as an Indicator of Near-Surface Ozone Sensitivity. *J. Geophys. Res. Atmos.* **2017**, *122*, 8885–8907. [[CrossRef](#)]
30. Stutz, J.; Kim, E.S.; Platt, U.; Bruno, P.; Perrino, C.; Febo, A. UV-Visible Absorption Cross Sections of Nitrous Acid. *J. Geophys. Res.* **2000**, *105*, 14585–14592. [[CrossRef](#)]
31. Bobrowski, N.; Hönninger, G.; Galle, B.; Platt, U. Detection of Bromine Monoxide in a Volcanic Plume. *Nature* **2003**, *423*, 273–276. [[CrossRef](#)] [[PubMed](#)]
32. Wagner, T.; Dix, B.; Friedeburg, C.V.; Frieß, U.; Sanghavi, S.; Sinreich, R.; Platt, U. MAX-DOAS O<sub>4</sub> Measurements: A New Technique to Derive Information on Atmospheric Aerosols—Principles and Information Content. *J. Geophys. Res. Atmos.* **2004**, *109*, D14203. [[CrossRef](#)]
33. Frieß, U.; Sihler, H.; Sander, R.; Pöhler, D.; Yilmaz, S.; Platt, U. The Vertical Distribution of BrO and Aerosols in the Arctic: Measurements by Active and Passive Differential Optical Absorption Spectroscopy. *J. Geophys. Res.* **2011**, *116*, D00R04. [[CrossRef](#)]
34. Wang, Y.; Dörner, S.; Donner, S.; Böhnke, S.; De Smedt, I.; Dickerson, R.R.; Dong, Z.; He, H.; Li, Z.; Li, Z.; et al. Vertical Profiles of NO<sub>2</sub>, SO<sub>2</sub>, HONO, HCHO, CHOCHO and Aerosols Derived from MAX-DOAS Measurements at a Rural Site in the Central Western North China Plain and Their Relation to Emission Sources and Effects of Regional Transport. *Atmos. Chem. Phys.* **2019**, *19*, 5417–5449. [[CrossRef](#)]
35. Liu, X.-H.; Zhang, Y.; Cheng, S.-H.; Xing, J.; Zhang, Q.; Streets, D.G.; Jang, C.; Wang, W.-X.; Hao, J.-M. Understanding of Regional Air Pollution over China Using CMAQ, Part I Performance Evaluation and Seasonal Variation. *Atmos. Environ.* **2010**, *44*, 2415–2426. [[CrossRef](#)]
36. Liu, X.-H.; Zhang, Y.; Xing, J.; Zhang, Q.; Wang, K.; Streets, D.G.; Jang, C.; Wang, W.-X.; Hao, J.-M. Understanding of Regional Air Pollution over China Using CMAQ, Part II. Process Analysis and Sensitivity of Ozone and Particulate Matter to Precursor Emissions. *Atmos. Environ.* **2010**, *44*, 3719–3727. [[CrossRef](#)]
37. Li, L.; An, J.Y.; Zhou, M.; Yan, R.S.; Huang, C.; Lu, Q.; Lin, L.; Wang, Y.J.; Tao, S.K.; Qiao, L.P.; et al. Source Apportionment of Fine Particles and Its Chemical Components over the Yangtze River Delta, China during a Heavy Haze Pollution Episode. *Atmos. Environ.* **2015**, *123*, 415–429. [[CrossRef](#)]
38. Vandaele, A.C.; Hermans, C.; Simon, P.C.; Carleer, M.; Colin, R.; Fally, S.; Mérianne, M.F.; Jenouvrier, A.; Coquart, B. Measurements of the NO<sub>2</sub> Absorption Cross-Section from 42,000 cm<sup>-1</sup> to 10,000 cm<sup>-1</sup> (238–1000 nm) at 220 K and 294 K. *J. Quant. Spectrosc. Radiat. Transf.* **1998**, *59*, 171–184. [[CrossRef](#)]
39. Serdyuchenko, A.; Gorshchev, V.; Weber, M.; Chehade, W.; Burrows, J.P. High Spectral Resolution Ozone Absorption Cross-Sections—Part 2: Temperature Dependence. *Atmos. Meas. Tech.* **2014**, *7*, 625–636. [[CrossRef](#)]
40. Volkamer, R.; Spietz, P.; Burrows, J.; Platt, U. High-Resolution Absorption Cross-Section of Glyoxal in the UV-Vis and IR Spectral Ranges. *J. Photochem. Photobiol. A Chem.* **2005**, *172*, 35–46. [[CrossRef](#)]
41. Fleischmann, O.C.; Hartmann, M.; Burrows, J.P.; Orphal, J. New Ultraviolet Absorption Cross-Sections of BrO at Atmospheric Temperatures Measured by Time-Windowing Fourier Transform Spectroscopy. *J. Photochem. Photobiol. A Chem.* **2004**, *168*, 117–132. [[CrossRef](#)]
42. Meller, R.; Moortgat, G.K. Temperature Dependence of the Absorption Cross Sections of Formaldehyde between 223 and 323 K in the Wavelength Range 225–375 Nm. *J. Geophys. Res. Atmos.* **2000**, *105*, 7089–7101. [[CrossRef](#)]
43. Chance, K.V.; Spurr, R.J.D. Ring Effect Studies: Rayleigh Scattering, Including Molecular Parameters for Rotational Raman Scattering, and the Fraunhofer Spectrum. *Appl. Opt.* **1997**, *36*, 5224. [[CrossRef](#)] [[PubMed](#)]
44. Wagner, T.; Beirle, S.; Brauers, T.; Deutschmann, T.; Frieß, U.; Hak, C.; Halla, J.D.; Heue, K.P.; Junkermann, W.; Li, X.; et al. Inversion of Tropospheric Profiles of Aerosol Extinction and HCHO and NO<sub>2</sub> Mixing Ratios from MAX-DOAS Observations in Milano during the Summer of 2003 and Comparison with Independent Data Sets. *Atmos. Meas. Tech.* **2011**, *4*, 2685–2715. [[CrossRef](#)]
45. Wang, Y.; Apituley, A.; Bais, A.; Beirle, S.; Benavent, N.; Borovski, A.; Bruchkouski, I.; Chan, K.L.; Donner, S.; Drosoglou, T.; et al. Inter-Comparison of MAX-DOAS Measurements of Tropospheric HONO Slant Column Densities and Vertical Profiles during the CINDI-2 Campaign. *Atmos. Meas. Tech.* **2020**, *13*, 5087–5116. [[CrossRef](#)]
46. Lin, J.C. Lagrangian Modeling of the Atmosphere: An Introduction. In *Lagrangian Modeling of the Atmosphere*; American Geophysical Union (AGU): Washington, DC, USA, 2012; pp. 1–11. [[CrossRef](#)]
47. Kim, J.; Jang, J.-A.; Oh, Y.-S.; Lee, H.; Joo, S.; Kim, S.; Boo, K.-O.; Lee, Y.G. Anthropogenic Carbon Dioxide Origin Tracing Study in Anmyeon-Do, South Korea: Based on STILT-Footprint and Emissions Data. *Sci. Total Environ.* **2023**, *894*, 164677. [[CrossRef](#)]
48. Lu, X.; Zhang, L.; Wang, X.; Gao, M.; Li, K.; Zhang, Y.; Yue, X.; Zhang, Y. Rapid Increases in Warm-Season Surface Ozone and Resulting Health Impact in China Since 2013. *Environ. Sci. Technol. Lett.* **2020**, *7*, 240–247. [[CrossRef](#)]
49. Ban, J.; Su, W.; Zhong, Y.; Liu, C.; Li, T. Ambient Formaldehyde and Mortality: A Time Series Analysis in China. *Sci. Adv.* **2022**, *8*, eabm4097. [[CrossRef](#)]
50. Ling, Z.H.; Zhao, J.; Fan, S.J.; Wang, X.M. Sources of Formaldehyde and Their Contributions to Photochemical O<sub>3</sub> Formation at an Urban Site in the Pearl River Delta, Southern China. *Chemosphere* **2017**, *168*, 1293–1301. [[CrossRef](#)]
51. Ren, B.; Xie, P.; Xu, J.; Li, A.; Qin, M.; Hu, R.; Zhang, T.; Fan, G.; Tian, X.; Zhu, W.; et al. Vertical characteristics of NO<sub>2</sub> and HCHO, and the Ozone Formation Regimes in Hefei, China. *Sci. Total Environ.* **2022**, *823*, 153425. [[CrossRef](#)]
52. Tian, X.; Xie, P.; Xu, J.; Li, A.; Wang, Y.; Qin, M.; Hu, Z. Long-Term Observations Of Tropospheric NO<sub>2</sub>, SO<sub>2</sub> and HCHO by MAX-DOAS in Yangtze River Delta Area, China. *J. Environ. Sci.* **2018**, *71*, 207–221. [[CrossRef](#)] [[PubMed](#)]

53. Xing, C.; Liu, C.; Hong, Q.; Liu, H.; Wu, H.; Lin, J.; Song, Y.; Chen, Y.; Liu, T.; Hu, Q.; et al. Vertical Distributions and Potential Sources of Wintertime Atmospheric Pollutants and the Corresponding Ozone Production on the Coast of Bohai Sea. *J. Environ. Manag.* **2022**, *319*, 115721. [[CrossRef](#)] [[PubMed](#)]
54. Hong, Q.; Zhu, L.; Xing, C.; Hu, Q.; Lin, H.; Zhang, C.; Zhao, C.; Liu, T.; Su, W.; Liu, C. Inferring Vertical Variability and Diurnal Evolution of O<sub>3</sub> Formation Sensitivity Based on the Vertical Distribution of Summertime HCHO and NO<sub>2</sub> in Guangzhou, China. *Sci. Total Environ.* **2022**, *827*, 154045. [[CrossRef](#)] [[PubMed](#)]
55. Lew, M.M.; Rickly, P.S.; Bottorff, B.P.; Reidy, E.; Sklaveniti, S.; Léonardis, T.; Locoge, N.; Dusanter, S.; Kundu, S.; Wood, E.; et al. OH and HO<sub>2</sub> radical chemistry in a midlatitude forest: Measurements and model comparisons. *Atmos. Chem. Phys.* **2022**, *20*, 9209–9230. [[CrossRef](#)]
56. Li, Z.; Smith, K.A.; Cappa, C.D. Influence of relative humidity on the heterogeneous oxidation of secondary organic aerosol. *Atmos. Chem. Phys.* **2018**, *18*, 14585–14608. [[CrossRef](#)]
57. Pan, L.; Xu, J.; Tie, X.; Mao, X.; Gao, W.; Chang, L. Long-Term Measurements of Planetary Boundary Layer Height and Interactions with PM<sub>2.5</sub> in Shanghai, China. *Atmos. Pollut. Res.* **2019**, *10*, 989–996. [[CrossRef](#)]
58. Wang, D.; Huo, J.; Duan, Y.; Zhang, K.; Ding, A.; Fu, Q.; Luo, J.; Fei, D.; Xiu, G.; Huang, K. Vertical Distribution and Transport of Air Pollutants during a Regional Haze Event in Eastern China: A Tethered Mega-Balloon Observation Study. *Atmos. Environ.* **2021**, *246*, 118039. [[CrossRef](#)]

**Disclaimer/Publisher’s Note:** The statements, opinions and data contained in all publications are solely those of the individual author(s) and contributor(s) and not of MDPI and/or the editor(s). MDPI and/or the editor(s) disclaim responsibility for any injury to people or property resulting from any ideas, methods, instructions or products referred to in the content.